ISIJ International, Vol. 41 (2001), No. 10, pp. 1262–1271

Comparison of Four Methods to Evaluate Fluid Velocities in a Continuous Slab Casting Mold

Brian G. THOMAS, Quan YUAN, Sivaraj SIVARAMAKRISHNAN, Tiebiao SHI, S. P. VANKA and Mohammad B. ASSAR[1)]

Deptartment of Mechanical and Industrial Engineering, University of Illinois, 1206 West Green Street, Urbana, IL 61801 USA. E-mail: bgthomas@uiuc.edu 1) LTV Steel Technology Center, Independence, OH 44131 USA.

(*Received on April 5, 2001: accepted in final form on July 4, 2001*)

Four different methods are compared for evaluating fluid flow velocities in the liquid pool in the mold region of a continuous caster of steel slabs. First, the instantaneous and time-averaged flow pattern in a 0.4-scale water model with single-phase flow is quantified using particle image velocimetry (PIV). Next, three-dimensional computations are performed to calculate the time-average flow pattern in the same system using a conventional finite-difference program, CFX, with the conventional K–ε model for handling turbulence. Transient computations are then performed using a 1.5-million node grid to resolve the turbulent eddies, both without a turbulence model (direct numerical simulation: DNS) and with a subgrid scale model (large eddy simulation: LES). Finally, measurements are obtained using electromagnetic sensors embedded in the mold walls of an operating steel slab casting machine. The comparisons reveal remarkable quantitative agreement between all four methods for the overall time-averaged flow pattern and surface velocities for these conditions. The time-averaged K–ε model is capable of accurate quantitative calculations of the steady flow field with the least effort, but has difficulty with transient behavior. The LES model predicts both steady and transient phenomena, but has severe computational cost. Water models with PIV are useful and practical tools, but are difficult to extend beyond the flow pattern to practical phenomena, such as heat transfer, solidification, surface slag entrainment, two-phase flow, and particle motion. The electromagnetic sensor has the advantage of measuring the real process, but is computed to be accurate only where the flow is roughly uniform and directly horizontally between the two probes, so is limited to measuring average speed at just a few points. Thus, each method has its own merits and disadvantages relative to the others, and can be a useful tool for investigating flow phenomena in processes with molten metal. Together, these methods reveal new insights into steady and transient flow in the continuous slab-casting mold, which are discussed in this work.

KEY WORDS: comparisons; steel; water model; transient fluid flow; numerical computations; K–ε turbulence equations; LES; large eddy simulation; PIV; particle image velocimetry; MFC; electromagnetic sensor; continuous caster.

1. Introduction

Flow in the mold region during the continuous casting of steel is of great interest because it influences many important phenomena, which have far-reaching consequences on strand quality. These include the flow and entrainment of the top surface powder/flux layers, top-surface contour and level fluctuations, and the entrapment of subsurface inclusions and gas bubbles. Flow in the mold can be studied using mathematical models, physical water models, and plant measurements. Scale water models have been applied with great success in previous work to study the flow of molten steel,[1–4)] owing to the similar kinematic viscosity of the two fluids, which governs much of the flow behavior. To better visualize and quantify the flow, Particle Image Velocimetry (PIV)[5)] has been applied recently to measure the instantaneous velocity fields in these water models.[6–8)] In this work, such measurements are performed on a water model at the LTV Technology Center (**Fig. 1**) using a PIV system supplied by DANTEC.[9)]

The turbulent flow through the nozzle and in the mold of the continuous caster has been studied extensively using computational models based on the Reynolds Averaged Navier Stokes (RANS) approach.[10–18)] The most popular of these are time-averaged models using the K–ε equations to model turbulence.[19)] In this work, the detailed evolution of the flow structures is also studied using the Large Eddy Simulation (LES) approach.[20)] LES is computationally much more intensive than K–ε, but offers a new level of insight into transient phenomena. In this work, the Origin 2 000 computers at the University of Illinois were used to perform K–ε simulations using CFX[21)] and LES simulations using LES3D.[22,23)]

Finally, flow can also be measured directly in the actual steel caster. A crude estimate of steel flow direction across the top surface can be obtained using the same measurement method used to monitor slag layer thickness. Specifically, the steel flow direction can be crudely estimated from the angle plowed up by the liquid steel as it flows around an inserted nail, as illustrated in **Fig. 2**. This angle

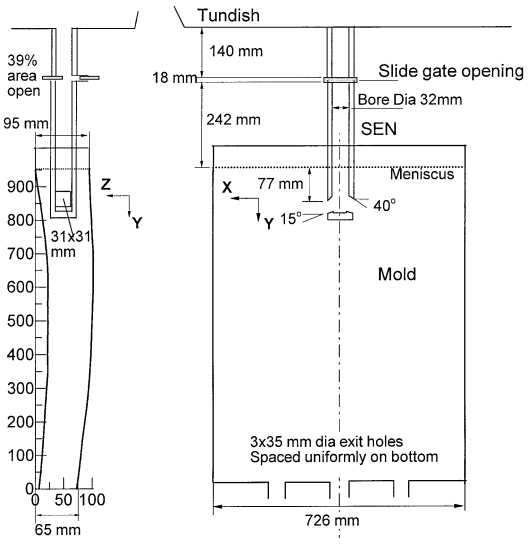

Fig. 1. Schematics of the 0.4-scale water model domain.

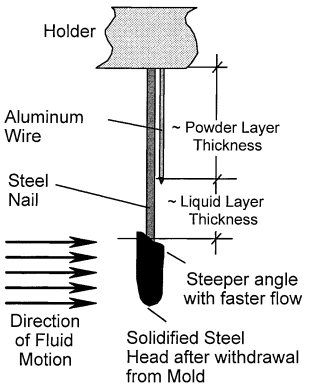

Fig. 2. Crude measurement of flux layer thickness and surface velocity.

steepens with increasing speed and can be captured as a frozen lump on the bottom of the nail, if care is taken. A more sophisticated method to measure surface velocities is to monitor the vibrations of a rod inserted into the flow through the top surface.[24] Another quantitative method measures an average molten steel velocity using electromagnetic (MFC) sensors embedded into the mold walls,[25,26] which monitor the electrical current generated when steel moves through a magnetic field. In this work, such measurements were obtained from MFC sensors installed at LTV Steel[7] by AMEPA GmbH.[25]

In this paper, all four of these methods are applied to quantify flow in the mold region of a continuous slab caster, for the same set of typical casting conditions and geometric parameters. The results are compared and applied to yield new insights into steady and transient flow phenomena in the continuous casting mold and into the relative merits of these tools to study them. This work is part of an ongoing effort to develop mathematical models of the continuous casting process and to apply them to increase understanding and solve problems of practical interest.

2. Water Model and PIV Measurements

The flow from the tundish passes through a slide gate, which moves at right angles to the wide face to restrict the opening in the nozzle and thereby control the flow rate. The flow then enters the mold cavity through the downward-angled square ports of the bifurcated nozzle, as shown in Fig. 1. Flow exits the bottom of the water model through three pipes attached to circular outlets in the bottom plate. **Table 1** lists the main dimensions and casting conditions used for this study. The thickness of the water model tapers from top to bottom in order to simulate only the liquid portion of the upper part of the steel caster.

Table 1. Water model conditions.

Tundish bath depth	400~410 mm
Nozzle length (total)	510 mm
UTN diameter	28 mm
Slide-gate diameter	28 mm
Slide-gate thickness	18 mm
Slide-gate orientation	90°
Slide-gate opening (FL)	52%
SEN submergence depth (top of port to top surface)	77± 3 mm
Bore (SEN) diameter	32 mm
Port width x height	31mm x 32mm
Port thickness	11 mm
Port angle, lower edge	15° down
Port angle, upper edge	40° down
Bottom well recess depth	4.8 mm
Water model length	950 mm
Water model width (steel caster width)	735 mm (72 in. full scale)
Water model thickness (steel caster thickness)	95 mm (top) to 65 mm (bottom) (9. in. full scale)
Outlets at bottom of mold domain (both halves)	3 round 35mm diameter outlets
Casting speed (model top)	0.633 m/min
Liquid flow rate through each port	3.53×10^{-4} m^3/s (5.6gal/min)
Average velocity at port	424 mm/s
Average jet angle at port	30° down
Liquid kinematic viscosity	1.0×10^{-6} m^2/s
Gas injection	0%

Flow visualization and velocity measurements were made using 0.4-scale Plexiglas water models of the tundish, nozzle and mold of the caster at LTV Steel Technology Center (Independence, OH). Sequences of instantaneous velocity measurements were obtained using a PIV system from DANTEC.[7,27] The positions of tracer particles are recorded digitally when two consecutive pulses of laser light illuminate a planar section through the water. Knowing the time interval between pulses (1.5×10^{-3} s) and the distances moved by the tracer particles (from image processing), a complete instantaneous velocity field is obtained. This procedure is usually repeated every 0.2 s and the results from at least 50 such exposures are averaged to obtain the time-averaged velocity field. Further details are given elsewhere.[7,27]

In order to get good resolution in the PIV measurements, the domain was divided into four regions: the vicinity near the nozzle ports, used to validate the inlet conditions, and three parts of mold, which were combined into a composite to illustrate the time-average flow pattern. The three parts are the top region containing the upper roll and the jet which has been averaged over 10 s (50 snapshots), the middle region containing the lower rolls (0.25–0.65 m below water surface) averaged over 200 s (200 snapshots), and the bottom region containing part of the lower roll and extending from 0.65–0.77 m averaged over 40 s (200 snapshots). The middle region is sometimes also a spatial average of the right and left half regions of the water model, in order

to average the considerable differences which arose due to asymmetry between sides.

3. Numerical Models

Several different numerical flow models were developed for this work at the University of Illinois. Each satisfies mass and momentum conservation in the computational domain by solving the continuity equation and the conservative form of the Navier Stokes equations for isothermal incompressible Newtonian fluids.

$$\frac{\partial v_j}{\partial x_j}=0 \quad \text{.....(1)}$$

$$\frac{\partial}{\partial t}\rho v_i+\frac{\partial}{\partial x_j}\rho v_j v_i=-\frac{\partial P}{\partial x_i}+\frac{\partial}{\partial x_j}\mu_{\text{eff}}\left(\frac{\partial v_j}{\partial x_i}+\frac{\partial v_i}{\partial x_j}\right) \quad \text{...(2)}$$

The solution yields the pressure, P, and velocity components, v_x, v_y, and v_z, at every point in the three-dimensional domain. Due to the nominal symmetry with respect to the centerline of the water model (and caster) shown in Fig. 1, only half of the model was simulated. The thickness variation was neglected. At the high flow rates involved, these models must account for turbulence, which is done through varying treatments of μ_{eff}.

3.1. K–ε Model

To solve Eqs. (1) and (2) on a computationally-efficient coarse grid using a time-averaged approximation, the conventional K–ε model averages the effect of turbulence over both time and space using an increased effective viscosity field, μ_{eff}:

$$\mu_{\text{eff}}=\mu_0+\mu_t=\mu_0+\rho C_\mu\frac{K^2}{\varepsilon} \quad \text{.....(3)}$$

where μ_0 and μ_t are the laminar and turbulent viscosity fields (kg/m·s) and C_μ is 0.09.[19] This approach requires solving two additional partial differential equations for the transport of turbulent kinetic energy, K (m^2/s^2), and its dissipation rate, ε (m^2/s^3):

$$\rho v_j\frac{\partial K}{\partial x_j}=\frac{\partial}{\partial x_j}\left(\frac{\mu_t}{\sigma_K}\frac{\partial K}{\partial x_j}\right)+\mu_t\frac{\partial v_j}{\partial x_i}\left(\frac{\partial v_i}{\partial x_j}+\frac{\partial v_j}{\partial x_i}\right)-\rho\varepsilon \quad \text{.....(4)}$$

$$\rho v_j\frac{\partial \varepsilon}{\partial x_j}=\frac{\partial}{\partial x_j}\left(\frac{\mu_t}{\sigma_\varepsilon}\frac{\partial \varepsilon}{\partial x_j}\right)+C_1\mu_t\frac{\varepsilon}{K}\frac{\partial v_j}{\partial x_i}\left(\frac{\partial v_i}{\partial x_j}+\frac{\partial v_j}{\partial x_i}\right)-C_2\frac{\varepsilon}{K}\rho\varepsilon \quad \text{.....(5)}$$

where the empirical constants, σ_K, σ_ε, C_1, and C_2 take standard values of 1.0, 1.3, 1.44, and 1.92[19] and i, j are coordinate direction indices, which when repeated in a term, implies the summation of all three possible terms. This approach needs special "wall functions" as the boundary conditions, in order to achieve reasonable accuracy on a coarse grid.[12,19,28] Inlet turbulence parameters at the inlet were fixed at average values for K of 0.044 m^2/s^2 and ε of 1.00 m^2/s^3, based on previous nozzle runs.

The equations were solved using the CFX v4.2 finite-volume CFD package.[21] The mold domain used 141 960 nodes, and converged (reducing relative residuals in velocity from 1 to about 0.01) in 1 200 iterations using constant under-relaxation factors of 0.4 for all variables except volume fraction and pressure, which were set to 1. To simplify the computational domain, only the mold was simulated without taper using a rigid wall for the top free surface. It required 2 hr of computation on a single SGI Origin 2000. The nozzle domain used 19 855 nodes and typically required 0.7 hr of computation. Further details are provided elsewhere.[27]

3.2. Large Eddy Simulation (LES) Model

Large Eddy Simulation (LES) uses a fine grid and small time steps to accurately capture details of the large-scale time-dependent structures of the flow. To obtain convergence, a turbulence model is often required to dissipate the kinetic energy at the sub-grid scale. The first of two LES simulations in this work, LES1, employed the Smagorinsky sub-grid-scale model[29]:

$$\mu_{\text{eff}}=\mu_0+\mu_t=\mu_0+0.01\rho(\Delta x\Delta y\Delta z)^{2/3}\sqrt{\frac{\partial v_i}{\partial x_j}\frac{\partial v_i}{\partial x_j}+\frac{\partial v_i}{\partial x_j}\frac{\partial v_j}{\partial x_i}} \quad \text{....(6)}$$

This LES1 simulation employed time- and position-varying velocities at the inlet plane which were taken from a separate LES solution of flow through an approximated nozzle geometry.[30] A 128×184×64 computational grid with over 1.5 million nodes was used with a time step of 0.0005 s. A second simulation, LES2, was performed by solving Eqs. (1) and (2) directly with no sub-grid scale turbulence model, so is sometimes referred to as DNS (direct numerical simulation). This simulation used the same grid, but obtained its transient inlet conditions from an LES solution of simple fully-developed turbulent flow in a square duct.[22] For both simulations, the inlet flow was directed into the domain at a downward angle of 30°.

The equations of both LES models are discretized using the Harlow–Welch fractional step procedure[31] on a staggered grid. Second order central differencing is used for the convection terms and the Crank Nicolson scheme[31] is used for the diffusion terms. The Adams–Bashforth scheme[31] is used to discretize in time with second order accuracy. The implicit diffusion terms are solved for using Alternate Line Inversion. The Pressure Poisson equation is solved using a direct Fast Fourier Transform solver. For parallelization, 1-D domain decomposition with MPI (Message Passing Interface) is used. The LES simulations are quite slow and take 18 CPU s per time step or 13 days (total CPU time) on an Origin 2000 (single processor) for each 60 s flow simulation.

4. Electromagnetic Sensor Measurements

The fourth method investigated in this work is the electromagnetic MFC sensor system to measure flow of molten steel, which was developed by AMEPA GmbH[25] and installed on the LTV Steel No. 1 slab caster in Cleveland to produce speed histories at four locations.[7] The MFC sensors can be used to determine whether the flow pattern in

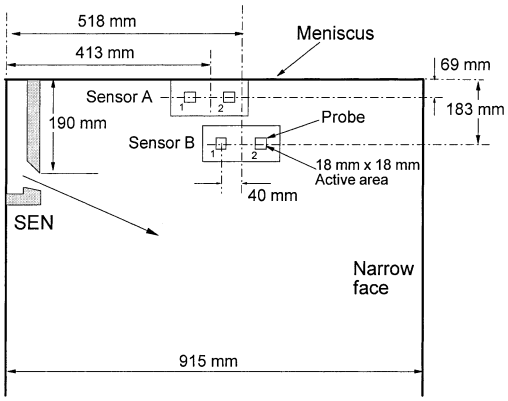

Fig. 3. Electromagnetic sensor locations (relative to steel caster dimensions).

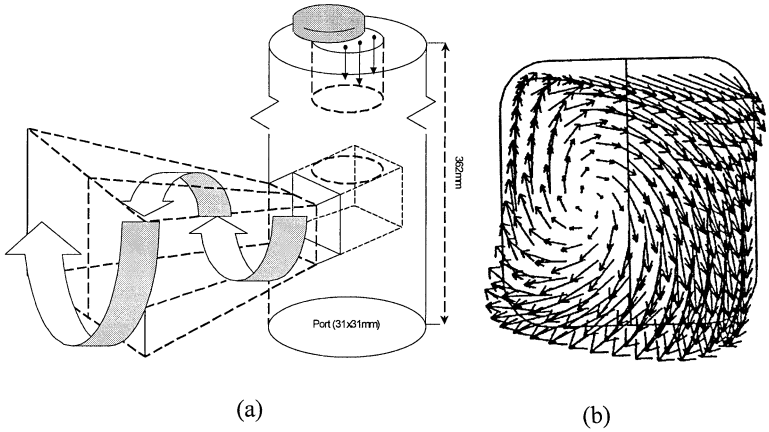

Fig. 4. Swirling flow exiting the nozzle: a) schematic based on PIV and b) secondary flow in the nozzle port plane calculated with K–ε.[27]

the molten steel has only a single roll or a lower and upper (double) roll.[7,25] The signals can also provide a measure of the strength of the velocities close to the top surface.

Each MFC sensor consists of two probes located close to each other behind the copper mold plates. Each probe consists of a permanent magnet and a detector. The flow of conducting steel through each associated magnetic field induces an electrical signal in each detector, according to Faraday's third law of electromagnetism. The time shift between prominent features of the two signals is a measure of the time taken by the flow to convect from one probe to the other. The average velocity in the region between the probes is then the distance between the probes divided by this time shift. This procedure is used because the absolute velocities at each probe are not known quantitatively with enough accuracy.

Figure 3 shows the location of two MFC sensors on half of the wideface of the mold. The geometry and conditions for the steel caster measurements were generally similar to those in the water model (Table 1), except for the full-scale 1 830 mm wide ×238 mm thick (72×9 inch) slab section size. Other minor differences include a uniform 15° downward port angle and a shallower average submergence depth (165–190 mm in the caster, or 66–77 mm in the model). Although argon gas is commonly injected into the real nozzle to help avoid clogging, no gas was employed during casting of the 61 slabs in this study.

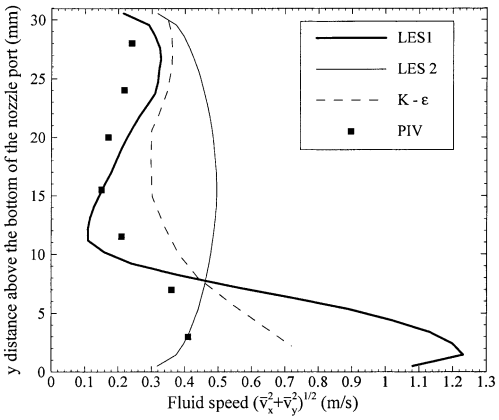

Fig. 5. Comparison of inlet velocity profiles along the centerline of the inlet port plane.

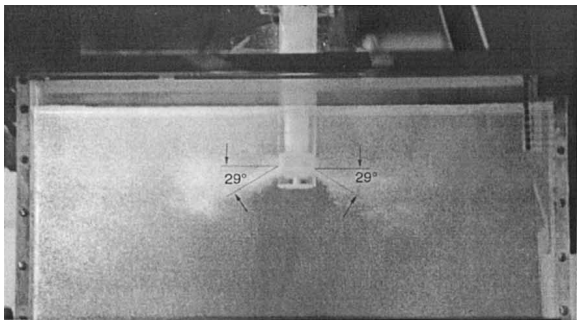

Fig. 6. Flow pattern and the average jet angle measurement in water model experiment.

5. Inlet Conditions from the Nozzle

Flow in the mold depends greatly on the inlet conditions, which are governed by the jet properties exiting the nozzle ports. Extensive studies of flow exiting the nozzle have been carried out in previous work.[12,14,18,27] The slide gate creates a strong swirl at the outlet ports of the nozzle, as shown in **Fig. 4**.[27] In both the simulation and the water experiments, the jet exits the ports with a single strong vortex or swirl, caused by asymmetric flow down the nozzle from the 90° slide gate orientation.[27]

No obvious "back-flow" into the nozzle port was observed during either the water model experiments or the simulations. This observation differs from many previous findings for typical nozzles,[12,14] including the nozzle employed in the steel plant. The lack of a back-flow-zone is mainly due to the special design of the SEN ports of this nozzle, which had a much steeper angle of the upper port edges (40° down) than the lower port edges (15° down).

Different inlet velocity profiles were adopted as inlet boundary conditions for the computational models of flow in the mold, as compared in **Fig. 5**. In addition to the modeling simplifications, the discrepancies are likely due in part to experimental error in manual alignment of the pulsed laser sheet along the nozzle centerline. Results using a simple turbulent profile based on pipe flow (LES2) were compared with 3-D distributions based on complete simulations of the nozzle (LES1 and CFX). All profiles have the same total outward mass flow, given in Table 1, and assume the same downward jet angle of 30°. This is similar to the

PIV measurement of 29° down, as seen in **Fig. 6** for Table 1 conditions but with 5.8% gas added to visualize the flow.[27] It is also similar to the 27.8° downward jet calculated from a CFX nozzle simulation for these conditions,[27] based on a weighted average over all nodes on the port plane. Nevertheless, uncertainty in the inlet profiles is an important source of discrepancies between the computations and measurements, which are discussed next.

6. Comparison of Mold Flow Patterns

Flow patterns derived from the water model PIV measurements, CFX, and LES simulations are compared in Figs. 6–11. **Figure 7** shows a side to side comparison of a typical instantaneous vector plot along the center plane of the water model, (parallel to the wide faces), obtained from the PIV measurements (left) and the LES2 simulation (right) for the conditions in Table 1. The swirling jet exiting the nozzle moves along a helical path across the mold, causing a characteristic jagged or "staircase-shaped" velocity vector pattern in the PIV measurements when viewed in a plane parallel to the wide faces. This flow feature fluctuates with time and is partly captured by the LES simulations, depending on the inlet conditions.[26] In both LES and PIV, the upper and lower roll structures each evolve chaotically between a single large recirculation structure and a complex set of evolving smaller structures and vortices. Strong evidence of this is also seen in the transient variations of the MFC sensor signals. Naturally, none of these phenomena can be seen in the time-averaged K–ε model results.

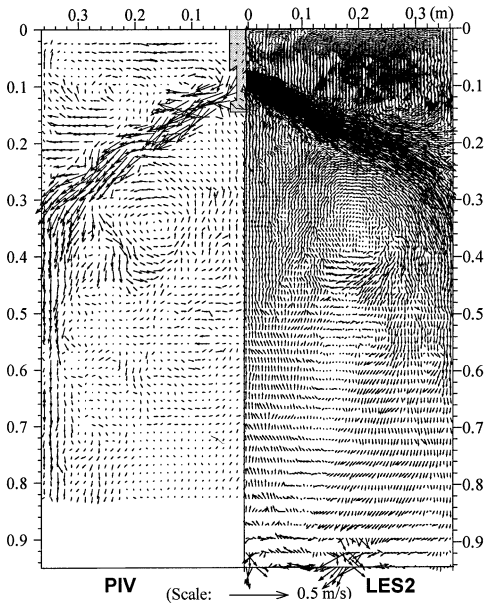

Fig. 7. Instantaneous velocity vector field at center plane between wide faces.

The corresponding time-averaged flow patterns are shown in **Fig. 8** to have a classic pair of simple recirculation zones in each half of the caster. They differ significantly from the instantaneous snapshots, which illustrates the limitations of time-averaging. The PIV, LES, and CFX time-averaged flow patterns are all quite similar in appearance. This demonstrates that the K–ε model can reasonably predict time-averaged flow in the mold, as known from previous study.[10,13]

Both the LES1, CFX, and PIV jets bend slightly upwards, as they traverse across the mold towards the narrow face. The LES2 simulation has a straighter jet and corresponding lower surface velocities, presumably due to neglecting swirl in the inlet condition. The straighter jet leads to more flow up the corners when the LES2 jet impacts the narrow face and spreads in all directions, as shown in **Fig. 9**. This causes lower velocities along a diagonal from the corner in the other section view shown in Fig. 8. It is interesting to note that this flow feature of LES2 is also found in the PIV measurements. Aside from this detail, all of the simulation and experimental flow patterns match fairly well.

Figure 10 is a 30-min time averaged vector plot of the velocities measured in both lower rolls of the water model. Considerable asymmetry can be seen between the left and right rolls, which persist even over this long time period. This is likely a feature of periodically unstable turbulent flow in the large cavity below the SEN, which has been previously observed[3,4] and calculated.[17] In addition, there may have been a slight (1°) misalignment of the nozzle in the X–Z plane. This may have moved the right-side jet out of

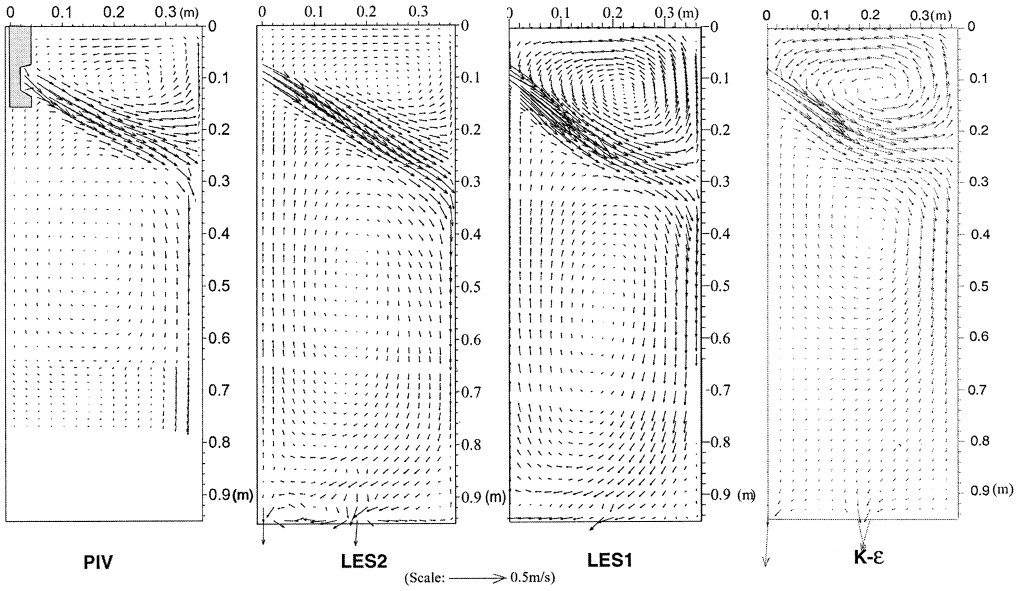

Fig. 8. Time averaged velocity field (center plane between wide faces).

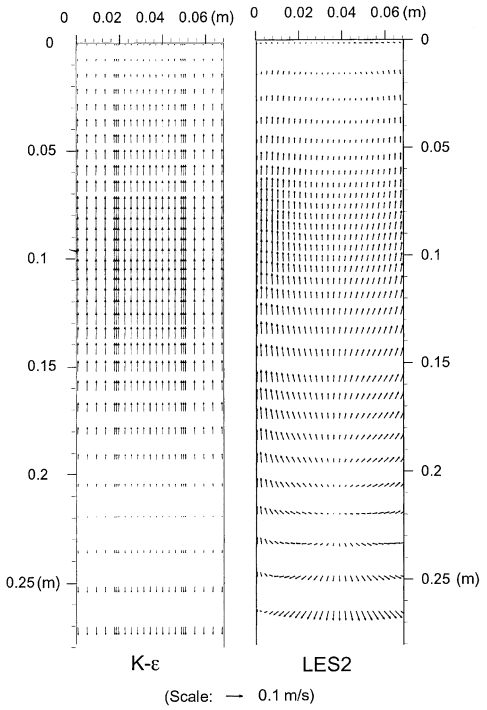

Fig. 9. Time-average velocity field on narrow face. (20 mm in from wall representing solidification front)

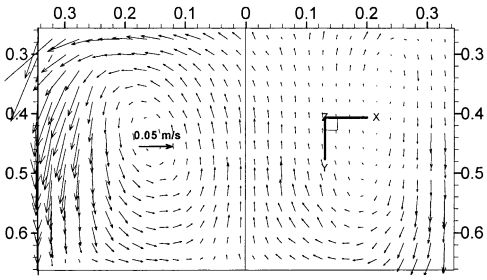

Fig. 10. PIV-measured velocity vectors in lower rolls. (30 min time average)

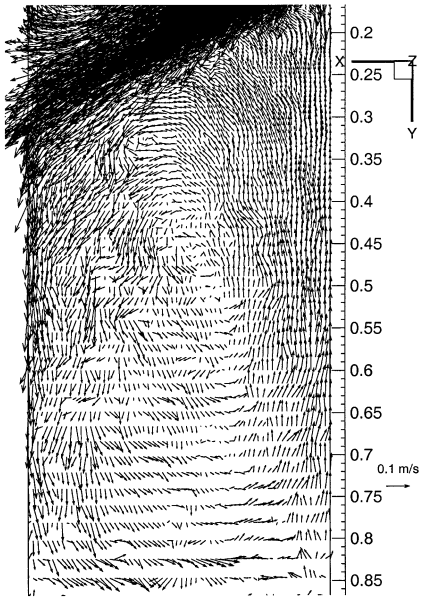

Fig. 11. Instantaneous LES2-simulation when lower roll is a large recirculation region.

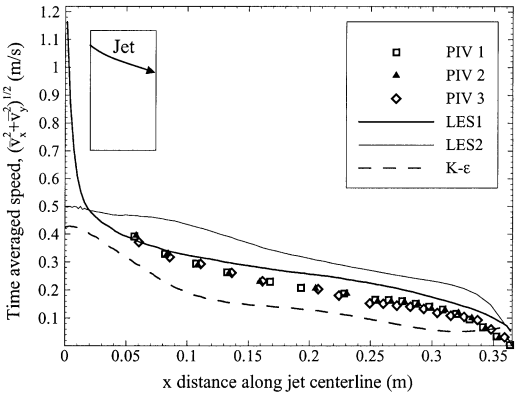

Fig. 12. Time-averaged speed profile along jet centerline, comparing PIV, *K*–*ε*, and LES.

the center plane and contributed to generally lower velocities on the right side. Proper simulation of these phenomena requires modeling the entire mold with no symmetry assumption.

Some features of the periodic evolution of the flow pattern measured in the water model are seen in the transient LES simulations as well. Figure 8(a) shows a short circuit structure that expands downward to form the single large recirculation region shown in **Fig. 11**. This matches a sequence of flow features measured with PIV and even has the same time scale (7–10 s). This suggests that this short circuit structure is probably caused by turbulence and not by changes at the inlet or by other disturbances which may be present in the PIV but not in the simulation. Some flow sequences between the lower rolls were observed in PIV to alternate over 45–60 s,[23] so were not simulated.

7. Comparison of Time-average Velocity Profiles

Quantitative comparisons of the PIV measurements with the *K*–*ε* and LES simulation results were made by plotting velocity profiles along three horizontal lines. **Figure 12** plots speed along the centerline of the jet. The three PIV data sets show close agreement, even though they were averaged over only 60 s each. The LES1 simulation matches closely with the PIV. The LES2 simulation naturally predicts slightly higher velocities on average, because its inlet condition produces a straighter jet with less out-of-plane motion. The *K*–*ε* prediction is low, perhaps owing to its overprediction of turbulence and the accompanying increase in the dissipation of the jet momentum.

Velocity across the top surface of the water model is shown in **Fig. 13** (taken about 1.5 mm below the meniscus). All three predictions agree with the PIV data. The greatest speeds are consistently found midway between the narrow face and the SEN. The LES2 predictions are slightly lower than the others, owing to the straighter jet producing less flow in the upper recirculation zone. This illustrates the importance of inlet conditions on the critical top-surface velocities.

Figure 14 shows the downward velocity profile across the width of the caster centerline, in the lower region, 0.6 m below the meniscus. The PIV measurements were time averaged over 2 000 s (2 000 frames), which reduced the variations between right and left sides shown in Fig. 10. For all cases, downward flow is naturally greatest along the narrow

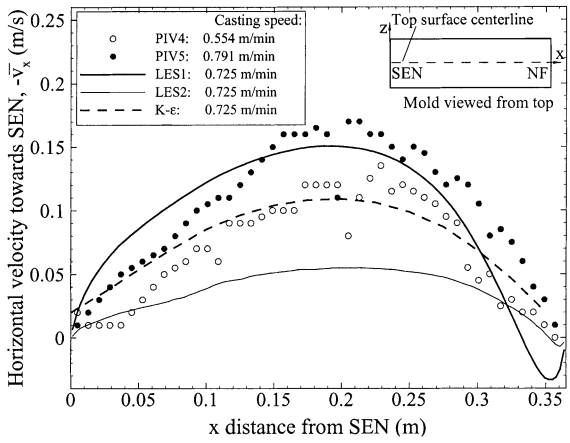

Fig. 13. Time-averaged speed profile along top surface centerline, comparing PIV, K–ε, and LES.

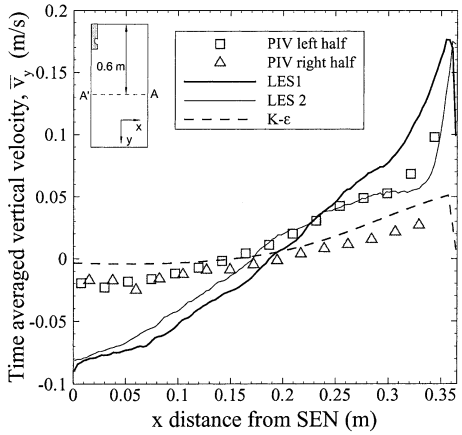

Fig. 14. Time-averaged speed profile along horizontal line 0.6 m below top surface, comparing PIV, K–ε, and LES.

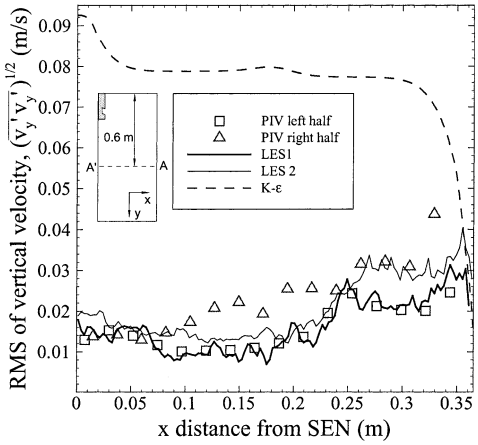

Fig. 15. Root mean square of turbulent variation in vertical velocity profile along horizontal line 0.6 m below top surface, comparing PIV, K–ε, and LES.

face walls. Quantitatively, the K–ε model produces the closest match. The LES simulations overpredict both the flow down the narrow face and the slow flow up the centerline. This is due in part to LES time averages of only 45 s. This is too short for the lower region, as indicated by large variations between the ten sets of 200 s each, which make up the PIV time average. In addition, the discrepancy might be due to neglecting the asymmetries due to mold curvature and left-to-right variations, or to inaccurate modeling of the outlet ports and bottom of the water model, which control

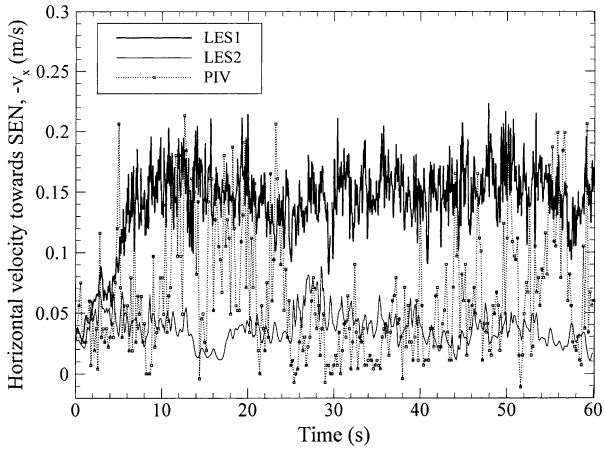

Fig. 16. Typical velocity history at the point half way between narrow face and SEN (about 2 cm below top surface), comparing PIV and LES simulation.

flow in the lower recirculation zones. In conclusion, all of the models appear to be capable of predicting reasonably accurate time-averaged behavior, if sufficient care is taken.

8. Comparison of Transient Behavior

Transient behavior is very important to quality in continuous casting and can be found even during periods of nominal steady-state conditions. Velocity variations can be characterized by their Root Mean Square variation, or RMS, which is defined in the PIV measurements and LES simulations by

$$\sqrt{\int_{t_1}^{t_2} (v_y - \bar{v}_y)^2 \, dt / \Delta t} \,,$$

where Δt is the interval for time averaging. The K–ε model is capable of only crude predictions of these time variations, by converting the isotropic turbulent kinetic energy into a mean velocity variation, RMS$=\sqrt{2K/3}$ assumed to be the same in each coordinate direction. These measures of velocity fluctuations are compared in **Fig. 15** along the same line and times as Fig. 14. They show that the LES simulations are remarkably accurate in quantifying this measure of transient variations due to turbulence. The K–ε model overpredicts the turbulent variations for this case. It is important to note the significant variation in RMS observed between the right and left sides of the PIV measurements.

Figure 16 shows a sample plot of time variation of velocity at a typical point 20 mm below the top surface, halfway between the SEN and the narrow face. The PIV velocity variation shows the existence of two time scales. The short time scale is about 0.7 s and is predicted well by the LES simulations. The longer time scale is at least 45 s. It results in periods of 5 s or more when the velocity close to the top surface is three to four times the mean. These long time-scale variations are of significant interest, as they would likely exacerbate shear entrainment of the liquid flux at the top surface and level fluctuations. The two LES simulations appear to bracket the extremes in the PIV measurements over long time scales. Thus, the long time-scale variations appear to be caused by differences in the penetration

depth of the jet. They might be due to long-time turbulent transients, to changes in the inlet conditions from the nozzle, or to side-to-side sloshing, which is neglected in the symmetry assumption of the simulation.

9. Comparison with Plant Measurements

9.1. LES Simulation of Electromagnetic Sensor

To enable comparisons of the MFC sensor signals with results from the other methods, LES2 simulation results were extracted to predict the output of the probes. As discussed in Sec. 4, the horizontal velocity component convects the flow structures from one probe to the other. Prominent flow features appear in both signals, with a time shift corresponding to the average horizontal velocity between the probes. To simulate this with the LES model, the horizontal velocity components calculated within the cells in the area beneath each probe head were first averaged in each plane parallel to the wideface. Next, the attenuation of the magnetic field strength with distance into the flow was taken into account by assuming that the induced signal strength decreased inversely with the square of the distance from the wideface, according to **Fig. 17**. Specifically, the overall simulated signal was calculated by taking a weighted average of the horizontal velocities calculated in the different planes beneath the probe head using the weighting factors in Fig. 17. Examination of the LES simulation results shows that variations through the mold thickness are less significant than the time variations, so the attenuation of the electromagnetic signal should not be important.

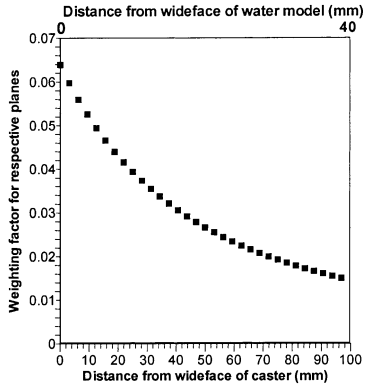

Fig. 17. Assumed weighting of velocities with distance from wideface by electromagnetic probes assumed for LES simulation.

Figures 18(a) and **18(b)** show typical simulated probe signals predicted for sensors A and B. The average of the two signals predicted at each probe indicates the best possible MFC sensor output. At position A, near the liquid surface, the two probe signals are very similar, except for an obvious time shift. Thus, it is quite feasible that the average of the two signals could be extracted by the signal processing logic, without knowing the absolute velocities shown on the vertical axis. At position B, however, the two probe signals are very different. Clearly, they do not always have the same basic signal offset in time, so it is very likely that large errors would arise in predicting their average by the signal processing.

The reason for this difference in behavior of the signals at A and B can be understood by looking at the flow fields near the two sensors. **Figure 19** shows two instantaneous velocity-vector plots in the top region. Flow at position A near the top surface is relatively consistent, as velocities are mainly horizontal and similar at both probes. Flow at position B is very different, however. The mean convection of vortices is not nearly horizontal. Flow past one probe often does not even reach the other probe. Thus, the two probe signals may not always correlate (Fig. 18(b)) and the derived sensor signal would likely show no relationship with the true velocity.

Figure 19 also shows how vortex structures traverse almost randomly across the caster, especially near the center of the upper rolls. Velocities predicted at sensor B probes indicate a real change in the direction of flow for several seconds (Fig. 18(b)) 122–124 s and 152–154 s). Even near Sensor A, the fluctuations appear to reverse the time shift for a few seconds (Fig. 18(a)) 70–72 s). Either of these situations might be falsely interpreted as a change between single and double roll patterns. In conclusion, this analysis suggests that the MFC sensor probes should be placed in regions of steady horizontal flow, such as found near the top surface. Moreover, temporary reversals in signal flow direction should be interpreted as local turbulent fluctuations

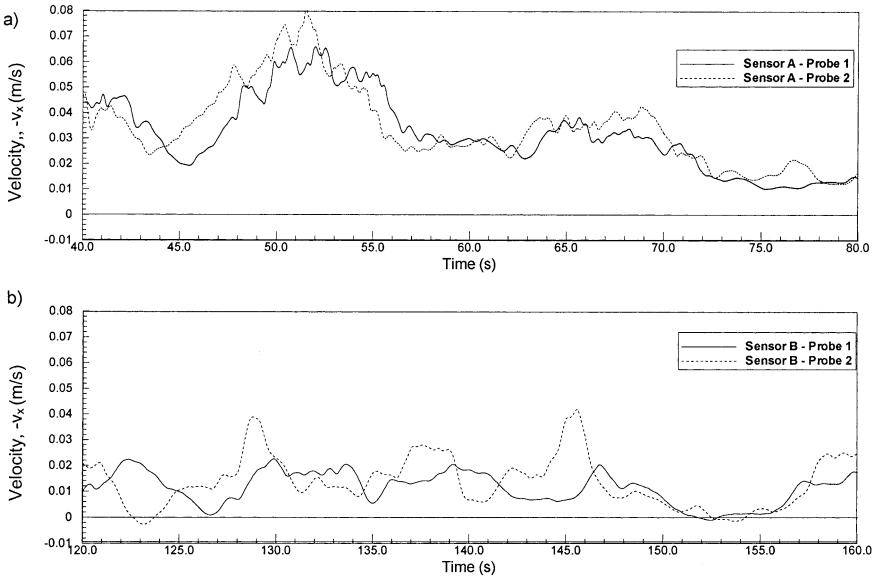

Fig. 18. LES-Simulated electromagnetic probe signals at locations A (a) and B (b).

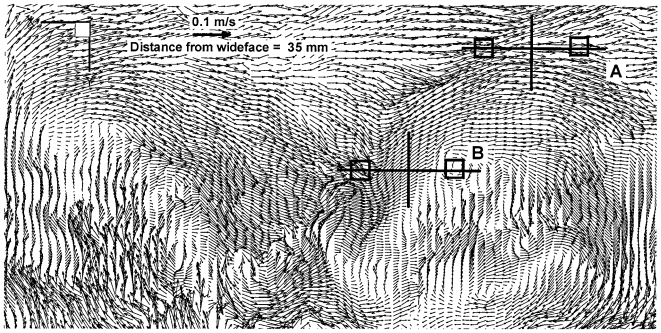

Fig. 19(a). Instantaneous LES-simulated vector plot of the upper roll 9mm from wideface.

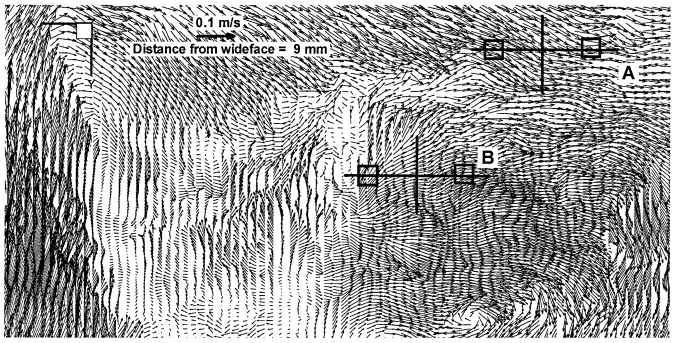

Fig. 19(b). Instantaneous LES-simulated vector plot of the upper roll 35 mm from wideface.

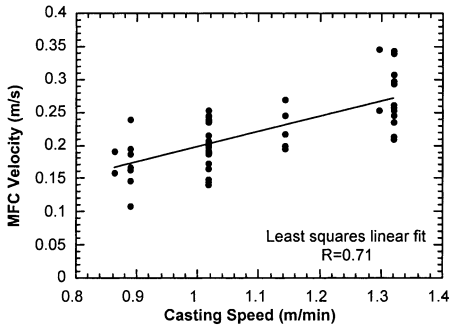

Fig. 20. Electromagnetic sensor output sorted by casting speed.[7)]

and do not necessarily indicate a real change in flow pattern.

9.2. Comparison with Electromagnetic Sensor Measurements

The gradually fluctuating shape of the signal recorded by the MFC sensors on the caster at LTV Steel is quite similar to the shape of the simulated probe signal in Fig. 18(a).[26)] **Figure 20** shows MFC output at A near the surface as a function of casting speed for Table 1 conditions. Each point is a 600 s time average. The significant scatter has several potential causes, including variations in casting conditions between the 61 slabs in the plant trial.

Qualitatively, the plant measurements agree with the other three flow analysis tools. The conditions under investigation always produce a classic double roll flow pattern, shown in Figs. 6 and 8. This is confirmed by both MFC sensors measuring flow towards the SEN. Maximum velocities along the top surface are found midway between the SEN and narrow face, and fluctuations are great. Top surface velocities increase with casting speed.

It is difficult to compare the MFC sensor data directly with the water model results in Fig. 13 due in part to the 0.4 scale factor. However, assuming Froude similarity means that the 0.725 m/min casting speed in the water model scales up by a factor of $\sqrt{1.0/0.4}$ to 1.15 m/min. in the caster. The average surface speed from the MFC sensor signal at 1.15 m/min is 0.23 m/s (Fig. 20). This agrees roughly with the average K–ε, LES1, and PIV value of 0.22 m/s (scaled up from the maximum of 0.14 m/s in Fig. 13). This agreement is very encouraging, but further validation is needed, especially when argon gas is present.

10. Summary

The turbulent flow of liquid steel in a continuous casting mold has been investigated with time-averaged K–ε and transient LES computational models. The predictions are compared both qualitatively and quantitatively with velocities measured using PIV on a 0.4-scale water model and with MFC sensor measurements in an operating steel caster. The results compare the abilities of these four methods, in addition to providing new insights into flow phenomena in this process.

10.1. Comparison of Methods

This work compares the relative merits of four tools to investigate the flow pattern and quantify fluid velocities. To obtain just the time-averaged flow pattern, the simple time-averaged K–ε model is both reasonably accurate and very cost-efficient. Transient phenomena are very complex and require several orders of magnitude more effort to investigate. The LES model is capable of accurately reproducing many transient phenomena, as demonstrated in this work. Even the jagged staircase flow caused by swirling flow exiting the nozzle ports can be predicted if the geometric features inside the nozzle are fully incorporated into the models. However, long-time transient phenomena, which are shown in the PIV work to be very important, are cost prohibitive to simulate with a conventional fine-grid LES model. Computational efficiency is further reduced by the need to avoid symmetry assumptions to study some phenomena. Thus, it appears to be infeasible to study many important transient phenomena with LES, even with state-of-the-art computer power.

Water models are very useful, practical tools for understanding and optimizing the flow pattern, especially when quantified using PIV. In addition, they can serve as educational tools for operator training. Their main drawback is the difficulty to extend beyond the flow pattern to phenomena of more practical interest, such as heat transfer, solidification, surface slag entrainment, two-phase flow, and particle motion.

The electromagnetic sensor has the advantage of measuring the real process, although it is expensive. The LES simulation of the MFC sensor signals illustrates the great importance of locating the sensor in a region of stable horizontal flow if accurate velocities are to be extracted. Sensors positioned near the top surface midway between narrow face and SEN should accurately output both the di-

rection and velocity history at that point. The individual probes of sensors positioned within a region of recirculating flow, however, experience very different transient flow fields, so cannot be relied upon to produce accurate velocities. This method is limited to measurements averaged over the region near each of just a few sensors. In summary, each method has its own merits and disadvantages relative to the others, and each can be a useful tool for investigating flow phenomena in processes with molten metal.

10.2. Insights into Transient Mold Flow

The numerical simulations, PIV and MFC results presented in this work together reveal deeper insight into flow in the continuous casting process, especially transient phenomena in the mold region. Strong swirl is generated at the port outlets by the 90°-oriented slide-gate nozzle. This causes considerable in and out of plane motion, which persists at least halfway across the mold. The flow pattern in the upper region of the mold evolves chaotically between a single large recirculation structure and a set of distinct vortices. Flow across the top surface varies in time by more than 100% of its mean value. This variation has a high frequency component (~1.5 Hz) which is also seen in the simulations, so appears to be inherent to the turbulent nature of the flow. The variations also include a low frequency component (time period of the order of 45 s) with times of more than 5 s when the horizontal velocities are 3–4 times larger than their mean values. This component is probably very significant to shear entrainment of liquid flux, level fluctuations, and the associated quality problems. It is not seen in the symmetric simulations with steady inlet conditions, which therein suggests the means to avoid it.

The inlet conditions to the mold from the nozzle are shown to be important for both steady and transient phenomena. Deeper penetration, such as resulting from less swirl at the inlet, impacts deeper along the narrow face, and lowers surface velocities and level fluctuations. Thus, it is useful to continue study to optimize nozzle design.

Although the entire geometry of the scale water model, including the inlet nozzle and its port were symmetric, there is considerable, persistent, asymmetry between the two lower rolls. Flow in the lower region alternates through different sequences of flow phenomena, which repeat chaotically and have longer time scales than the upper zone. One of these features involves a short circuit between the upward and downward flow in the lower roll and evolves over 7–10 s. This phenomenon is also seen in the simulation and appears to be inherent to the turbulent nature of the flow. Some flow asymmetries in the lower rolls alternate periodically over 45–60 s, while others may persist for very long periods of time (one hour or more).

Transient flow phenomena are likely very important to inclusion particle motion and bubble entrapment, which are responsible for defects in the final product. Thus, further study of transient flow phenomena using all four tools studied in this work should be a fruitful research area for continuous casting of steel and other processes involving molten metal flow.

Acknowledgements

The authors would like to thank the National Science Foundation (NSF-Grant # DMI-98-00274) and the Continuous Casting Consortium (CCC) at the University of Illinois at Urbana Champaign (UIUC) for their support of this research, the National Center for Supercomputing Applications (NCSA) at the UIUC for computing time, AEA technology for use of the CFX 4.2 program, and LTV Steel, especially Pierre Dauby, for use of the water model and PIV system and access to PIV and MFC measurements.

REFERENCES

1) L. J. Heaslip and J. Schade: *Iron Steelmaker* (*ISS Transactions*), **26** (1999), No. 1, 33.
2) J. Herbertson, Q. L. He, P. J. Flint and R. B. Mahapatra: Steelmaking Conf. Proc., Vol. 74, ISS, Warrendale, PA, (1991), 171.
3) T. Honeyands and J. Herbertson: *Steel Res*., **66** (1995), No. 7, 287.
4) D. Gupta and A. K. Lahiri: *Metall. Mater. Trans. B*, **27B** (1996), No. 5, 757.
5) C. E. Willert and M. Gharib: *Experiments in Fluids*, **10** (1991), No. 4, 181.
6) D. Xu, W. K. Jones and J. W. Evans: Processing of Metals and Advanced Materials: Modeling, Deisgn and Properties, eds. by B.Q. Li, TMS, Warrendale, PA, (1998), 3.
7) M. B. Assar, P. H. Dauby and G. D. Lawson:, Steelmaking Conf. Proc., Vol. 83, ISS, Warrendale, PA, (2000), 397.
8) I. Lemanowicz, R. Gorissen, H.-J. Odenthal and H. Pfeifer: *Stahl Eisen*, **120** (2000), No. 9, 85.
9) Dantec Flow Technology: User's Guide, V. 2.01, Mahwah, New Jersey, (1998).
10) B. G. Thomas, L. J. Mika and F. M. Najjar: *Metall. Trans. B*, **21B** (1990), No. 2, 387.
11) N. Bessho, R. Yoda, H. Yamasaki, T. Fujii, T. Nozaki and S. Takatori: *Iron Steelmaker* (*ISS Transactions*), **18** (1991), No. 4, 39.
12) D. E. Hershey, B. G. Thomas and F. M. Najjar: *Int. J. Numerical Methods in Fluids*, **17** (1993), No. 1, 23.
13) B. G. Thomas, X. Huang and R. C. Sussman: *Metall. Trans. B*, **25B** (1994), No. 4, 527.
14) F. M. Najjar, B. G. Thomas and D. E. Hershey: *Metall. Trans. B*, **26B** (1995), No. 4, 749.
15) M. R. Aboutalebi, M. Hasan and R. I. L. Guthrie: *Metall. Mater. Trans. B*, **26B** (1995), No. 4, 731.
16) A. Theodorakakos and G. Bergeles: *Metall. Mater. Trans. B*, **29B** (1998), No. 6, 1321.
17) X. Huang and B. G. Thomas: *Can. Metall. Q*., **37** (1998), No. 304, 197.
18) H. Bai and B. G. Thomas: *Metall. Mater. Trans. B*, **32B** (2001), No. 2, 269.
19) B. E. Launder and D. B. Spalding: *Computer Methods in Applied Mechanics and Engr*, **13** (1974), No. 3, 269.
20) R. Rogallo and P. Moin: *Ann. Rev. Fluid Mechanics*, **16** (1984), 99.
21) CFX 4.2: AEA Technology, Pittsburgh, PA, Report, (1998).
22) R. Madabushi and S. P. Vanka: *Physics of Fluids*, **3** (1991), No. 11, 2734.
23) S. Sivaramakrishnan: M. S. Thesis, University of Illinois, (2000).
24) H. Mizukami, M. Hanao, S. Hiraki, M. Kawamoto, T. Watanabe, A. Hayashi and M. Iguchi: *Tetsu-to-Hagané*, **86** (2000), No. 4, 265.
25) K. U. Kohler, P. Andrzejewski, E. Julius and H. Haubrich: Steelmaking Conf. Proc., Vol. 78, ISS, Warrendale, PA, (1995), 445.
26) S. Sivaramakrishnan, H. Bai, B. G. Thomas, P. Vanka, P. Dauby and M. Assar: Ironmaking Conf. Proc., Vol. 59, ISS, Warrendale, PA, (2000), 541.
27) H. Bai and B. G. Thomas: *Metall. Mater. Trans. B*, **32B** (2001), No. 2, 253.
28) B. G. Thomas and F. M. Najjar: *Appl. Math. Model.*, **15** (1991), No. 5, 226.
29) J. Smagorinsky: *Monthly Weather Review*, **91** (1963), 99.
30) B. G. Thomas: Continuous Casting Consortium, University of Illinois at Urbana-Champaign, Report, (2000).
31) J. Tannehill, D. Anderson and R. Pletcher: Computational Fluid Dynamics and Heat Transfer, Taylor and Francis, Washington, DC, (1997).